Electronic Supplementary Material (ESI) for Catalysis Science & Technology.

# Electronic Supplementary Information

# Catalytic Decomposition of Methane into Hydrogen and High-Value Carbons: Combined Experimental and DFT Computational Study

I-Wen Wang[a], Robert A. Dagle[b], Tuhin Suvra Khan[c], Juan A. Lopez-Ruiz[b], Libor Kovarik[b], Yuan Jiang[b], Mengze Xu[b], Yi Wang[d], Changle Jiang[a], Stephen D. Davidson[b], Pedram Tavadze[e], Lili Li[f,*], and Jianli Hu[a,*]

[a] Department of Chemical & Biomedical Engineering, West Virginia University, Morgantown, WV 26506, USA.

[b] Institute for Integrated Catalysis, Pacific Northwest National Laboratory, 902 Battelle Blvd Richland, WA 99352, USA.

[c] Light Stock Processing Division, CSIR-Indian Institute of Petroleum, Dehradun 248005, India.

[d] Department of Mechanical & Aerospace Engineering, West Virginia University, Morgantown, WV 26506, USA

[e] Department of Physics, West Virginia University, Morgantown, WV 26506, USA

[f] College of Life Science and Agronomy, Zhoukou Normal University, Zhoukou, Henan, China

*Corresponding authors: Tel: (304)293-5067. Email: john.hu@mail.wvu.edu;

Tel: (86)13672165360. Email: 13672165360@163.com

## S1. Additional catalyst characterization

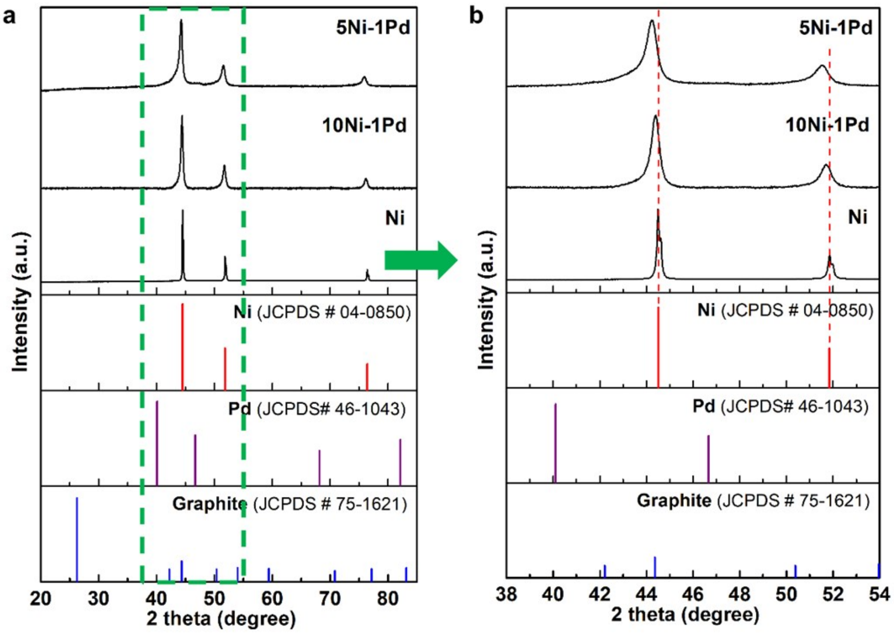

**Fig. S1.** X-Ray diffraction (XRD) patterns of as-reduced unsupported catalysts. **a)** 5Ni-1Pd, 10Ni-1Pd, and Ni; the standard spectrums of graphite, metallic Pd and Ni. **b)** The magnification of the scale from 38° to 54°.

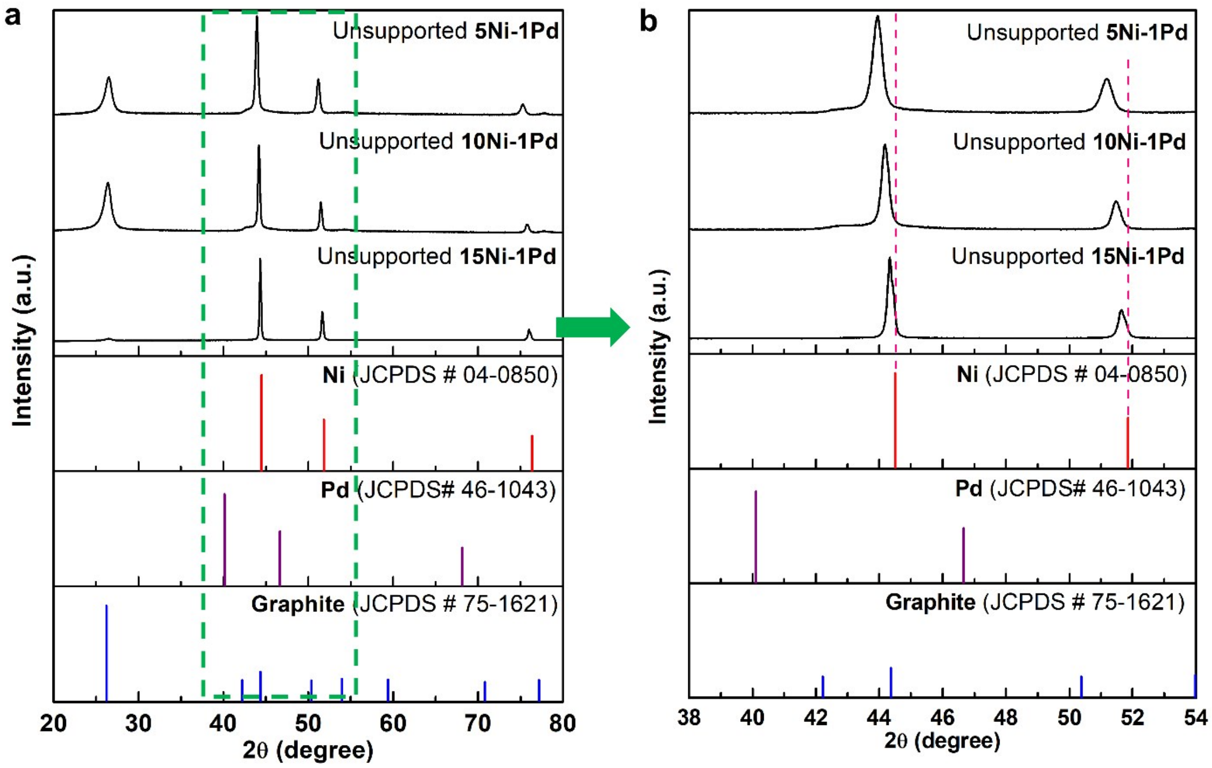

**Fig. S2.** X-Ray diffraction (XRD) patterns of spent unsupported catalysts. **a)** Two thetas between 20-80° **b)** The magnification of the scale from 38° to 54°.

The XRD results of spent unsupported catalysts after the TCD reaction were shown in Fig S2. The characteristic peak of graphitic carbon (JCPDS # 75-1621) is observed on the spent 10Ni-1Pd and 5Ni-1Pd and due to the absence of CNT support we can confirm the peak appeared after the formation of carbon. The intensity of carbon peak is consistent with their higher methane conversion compared to the low conversion of 15Ni-1Pd on which carbon peak is barely observed. The formation of an alloy catalyst is consistent with STEM results.

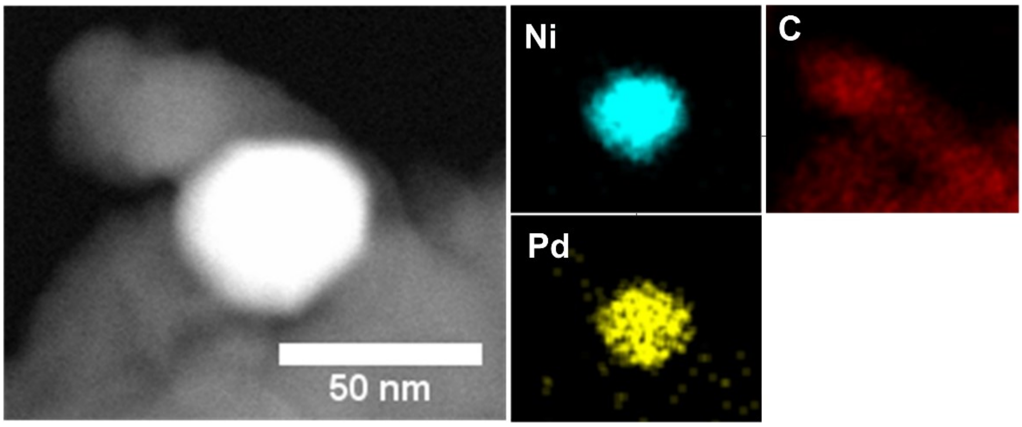

**Fig. S3.** The STEM-EDS mapping of spent 10Ni-1Pd/CNT

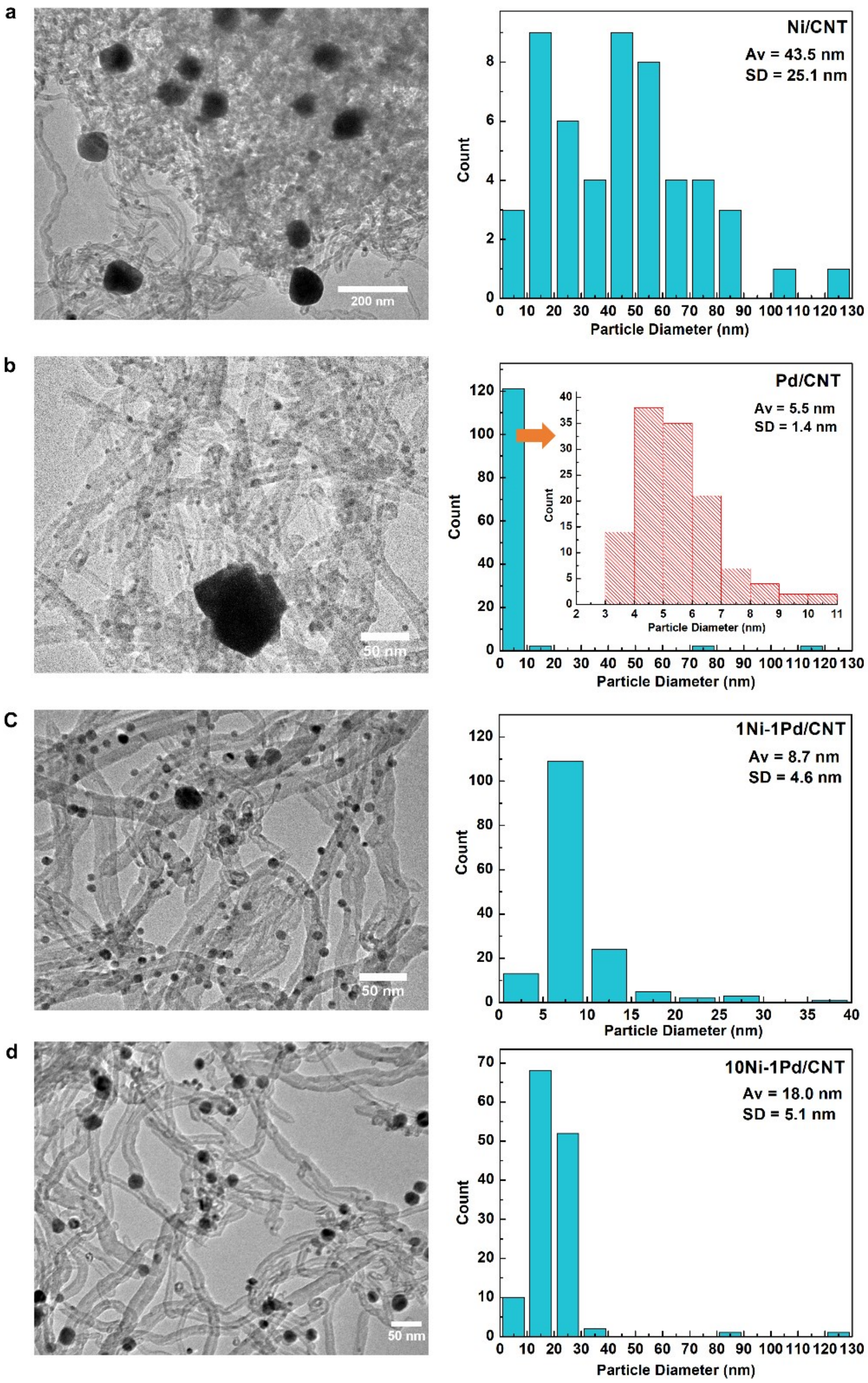

**Fig. S4.** Transmission electron microscopy (TEM) images of fresh-reduced catalysts and particle size distribution for different catalysts where **a)** represents Ni/CNT. **b)** represents Pd/CNT. **c)** represents 1Ni-1Pd/CNT and **d)** represents 10Ni-1Pd/CNT.

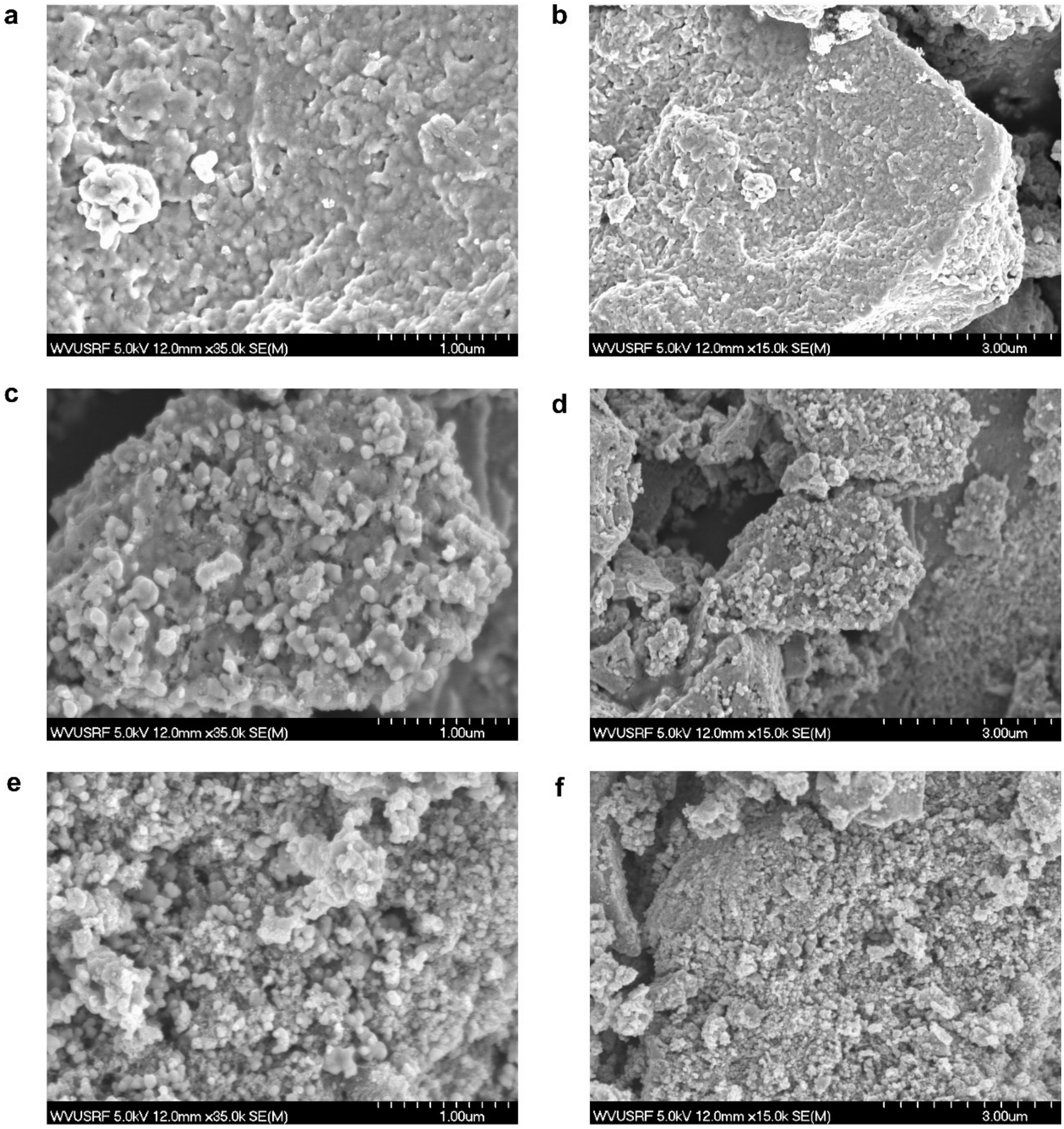

**Fig. S5.** Scanning electron microscopy (SEM) images of fresh-reduced unsupported catalysts with different magnifications where: **a and b)** represent Ni **c and d)** represent 15Ni-1Pd and **e and f)** represent 10Ni-1Pd.

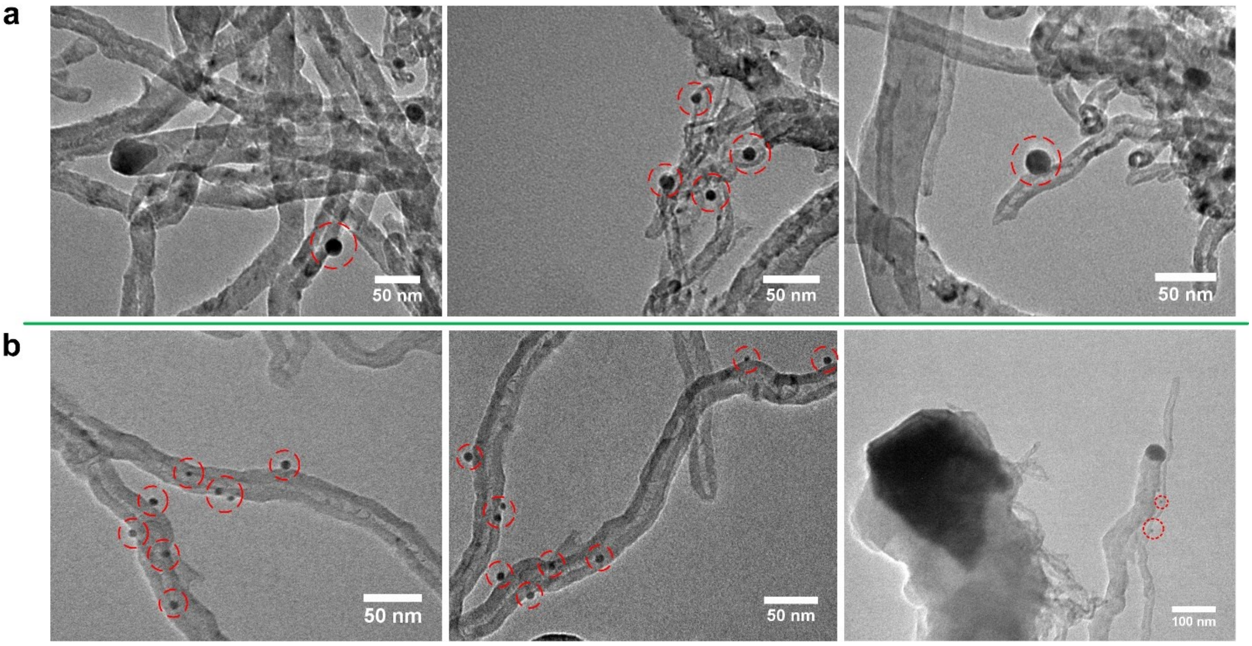

**Fig. S6.** TEM images of spent catalysts where **a)** represents 10Ni-1Pd/CNT and **b)** represents Pd/CNT.

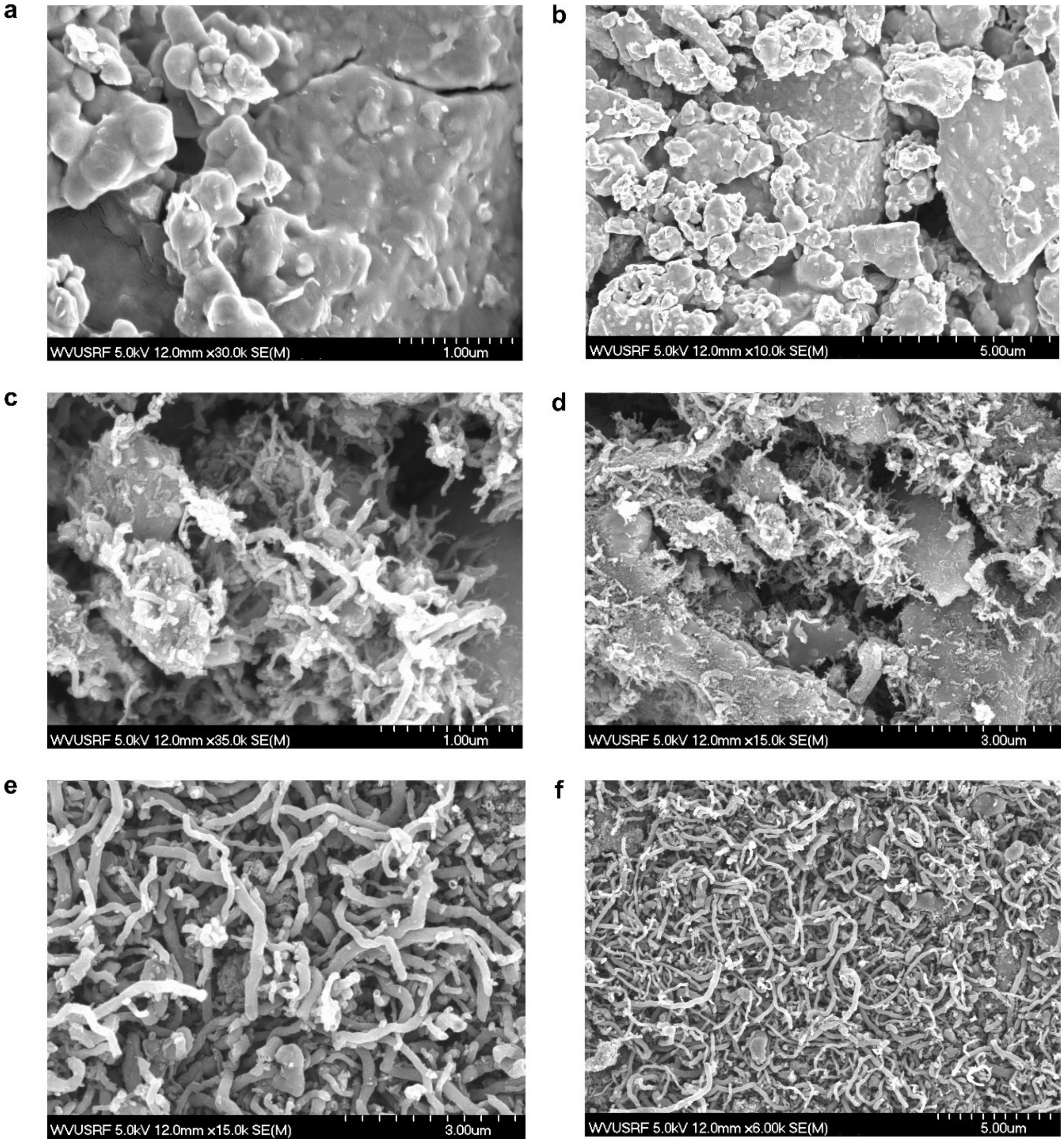

**Fig. S7.** SEM images of unsupported catalysts after reaction with different magnifications where **a and b)** represent Ni, **c and d)** represent 15Ni-1Pd, and **e and f)** represent 10Ni-1Pd.

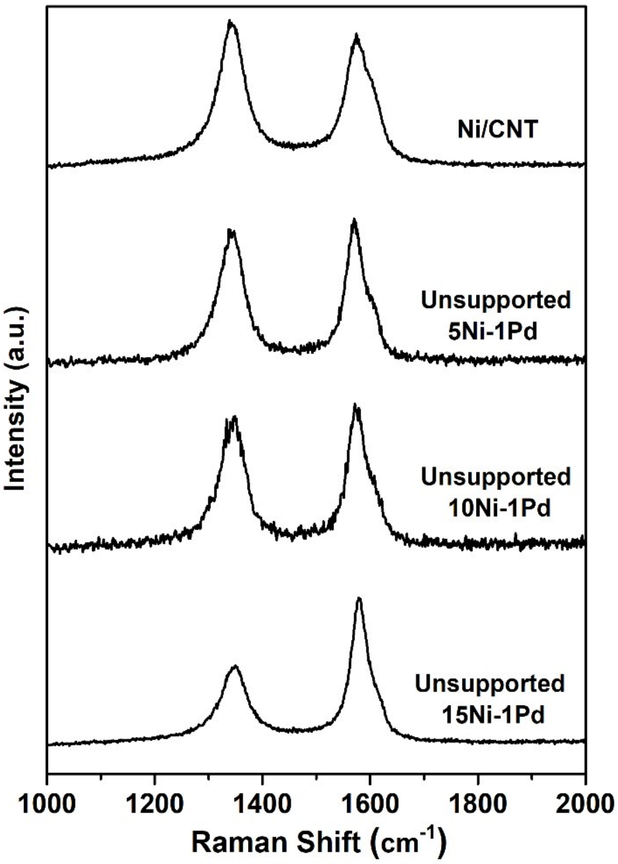

**Fig. S8.** Raman patterns of spent Ni/CNT, and spent unsupported 5Ni-1Pd, 10Ni-1Pd, and 15Ni-1Pd.

## S2. Density functional theory (DFT) calculations and ab-initio microkinetic modeling (MKM)

To calculate the initial $CH_4$ decomposition conversion trends over the transition metals, an ab-initio microkinetic model (MKM) was designed for $CH_4$ decomposition over (111) surface of transition metals – Ag, Cu, Pt, Pd, Ni, Ru and Rh using the descriptor-based analysis platform in CatMAP[1-3], developed at Stanford University. The steady-state solutions of the differential rate equations are obtained using a multi-dimensional Newton's root finding method as implemented in CatMAP. Further details of the MKM methodology are given by Grabow et al.[4] and in our previous publications [5-7]. The elementary steps involved are given below in Eq. S1 to S6.

R1: $CH_4(g) + 2^* \rightarrow CH_3^* + H^*$ Equation S1

R2: $CH_3^* + {}^* \rightarrow CH_2^* + H^*$ Equation S2

R3: $CH_2^* + {}^* \rightarrow CH^* + H^*$ Equation S3

R4: $CH^* + H^* \rightarrow C^* + H^*$ Equation S4

R5: $C^* + C^* \rightarrow C_2^* + {}^*$ Equation S5

R6: $H^* + H^* \rightarrow H_2(g) + 2^*$ Equation S6

R6: $3\ C_2^* \rightarrow C_6(g) + 3^*$ Equation S6

where the (g) refers to gas-phase species, A* refers to species A adsorbed at the transition metal (111) surface, and * means a free active site at (111) surface.

Energies of the adsorbed species, transition state over the transition metal surfaces used in the kinetic model were obtained from the CatApp database[8]. These energies were calculated using similar plane wave DFT calculations with Generalized Gradient Approximation (GGA) of Revised Perdew-Burke-Ernzerhof (RPBE) exchange-correlation functional. Energies of the intermediates and transition states were referenced to the gas phase energies of $H_2$ and $CH_4$ using Eq. S7.

$$E_{CxHy} = E_{slab + CxHy} - E_{slab} - [\ x(E_{CH4} - 2E_{H2}\ ) + y/2\ E_{H2}] \qquad \text{Equation S7}$$

where $E_{slab\ +\ CxHy}$, $E_{CH4}$ , $E_{H2}$, $E_{slab}$ are the energies of adsorbed intermediate, methane, hydrogen, and clean surface, respectively.

Energies of the $CH_x$ adsorbed species and $CH_x$-H bond dissociation transition state over the Ni(111) and Pd(111) surfaces were obtained from the CatApp database[8]. The energies of adsorbed $C_2$ over the Ni(111) and Pd(111) and $Ni_3Pd$(111) surfaces were calculated using the DFT method discussed in the Computational Methods section. The energetics of C-C coupling transition state is obtained using the BEP scaling relationship by Falsig et al.[9]. As can be seen in Fig. 6a, all the three catalyst surfaces have similar energy profiles with similar activation barriers for C-H bond dissociation and C-C coupling reaction. The activation barrier ($E_{act}$) for the first C-H bond activation for Ni (111) and Pd (111) was calculated to be 1.27 eV and 1.13 eV, respectively, whereas the barrier at the $Ni_3Pd$ surface was calculated to be little higher 1.35 eV. The adsorbed $CH_3$ and $CH_2$, dissociated with a lower barrier; 0.8 eV, 1.03 eV and 1.02 eV for Ni(111), Pd(111) and $Ni_3Pd$(111) surface, respectively, for C-H bond dissociation of $CH_3$; whereas for C-H bond dissociation of $CH_2$ adsorbate the barriers calculated to be 0.34 eV, 0.6 eV and 0.61 eV for Ni(111), Pd(111) and $Ni_3Pd$(111) surface, respectively. The activation barrier for C-H bond dissociation of adsorbed CH intermediate is calculated to be higher for Ni(111) and Pd(111), 1.39 eV and 1.38 eV, respectively, compared to the one observed over $Ni_3Pd$(111) surface, 1.09 eV. The highest activation barriers calculated for the methane C-H bond dissociation over Ni (111), Pd(111) and $Ni_3Pd$ (111) are 1.39 eV, 1.38 eV and 1.35 eV, respectively, are all of similar value. Hence, from the methane C-H bond dissociation energy diagram shown in Fig. 6a, it is difficult to explain the higher initial conversion of methane over

Ni compared to Pd and Ni-Pd catalysts. The formation of $C_2$ species at the metal surface is an integral step towards the graphitic and amorphous coke formation [10-12]. The activation energy for C-C coupling reaction over three metal surfaces also has similar barriers, 1.06 eV, 1.04 eV, and 1.14 eV, for Ni(111), Pd(111), and $Ni_3Pd$(111), respectively. However the formation of $C_2$ species ($C_2$+8H) is more favorable over the Ni(111) surface (1.42 eV), compared to the Pd(111) and $Ni_3Pd$(111) surface (2.12 eV and 1.82 eV, respectively), as shown in Fig. 6a, which can lead towards higher initial methane conversion for the Ni catalyst, as seen in the experiments.

The entropies of the gas-phase species were described using the Fixed entropy assumption [1,4], whereas zero point energy (ZPE) were obtained using the normal mode vibrational frequencies. Entropy and ZPE values of the gas-phase molecules are given in Table S1. The adsorbates entropies were assigned to zero using the Frozen adsorbate approximation [13]. Two different adsorption sites, one for hydrogen and one for all the other adsorbates in the MKM model [5,7,14]. Here in the MKM models, the number of two different sites are kept equal. The adsorption energy and transition state scaling [1,15,16] relationships used in the model has been shown in Fig. S9. In order to simulate reactor operational conditions, the solutions for the MKM were obtained for reaction conditions at temperature 600 °C and pressure 1 bar, with 0.01% conversion of methane.

**Table S1.** Formation energy, entropy, and ZPE of the reactant and product gas-phase species.

Note: Energy of $C_6$ is obtained from the ΔH of reaction: $CH_4 \rightarrow C + 2H_2(g)$ $\Delta H_r = 74.87$ kJ/mol [17,18].

| Gas-phase species | Formation Energy (eV) | Entropy (eV/K) | ZPE ($cm^{-1}$) |
|---|---|---|---|
| $CH_4$ | 0 | 0.00193 | 9828 |
| $H_2$ | 0 | 0.00135 | 2233 |
| $C_6$(coke) | 4.66 | 0.0001 | 32343 |

MKM coverage analysis:

The coverage analysis performed to obtain the coverages of adsorbed species at the transition metals (111) surfaces are shown in Fig. S11. Among the transition metals, Cu does not have appreciable coverage (< 0.1 ML) of any adsorbate, as shown in Fig. S11, indicating towards the noble nature and low reactivity for methane dissociation. Reactive transition metals Ru and Rh are found to have high coverage of C (0.3 ML and 0.2 ML, respectively), followed by Pt (0.1 ML), whereas the C coverage are negligible over Pd, $Ni_3Pd$ and Ni surfaces (<0.1 ML), as can be seen in Fig. S11a. Among the transition metals only Ru and Ni have significant coverage of $C_2$, 0.3 ML, and 0.1 ML, respectively, as can be seen in Fig. S11b. Coverage of CH (Fig. S11c) is found to be significant over most of the transition metals, with Pt having the highest CH coverage of 0.8 ML, followed by Rh with 0.7 ML. Ni, Pd, $Ni_3Pd$ and Ru also show appreciable coverage of CH, 0.3 ML, 0.2 ML, 0.6 ML, and 0.5 ML, respectively. The high coverages of CH species over the transition metals can be correlated to the high C-H activation barrier for transition metal (111) surface, as can be seen in Fig. 6a for Ni and Pd. Fig. S12 illustrates rate volcano plot for coke and $H_2$ production over transition metal surfaces plotted against the C and $C_2$ binding energy.

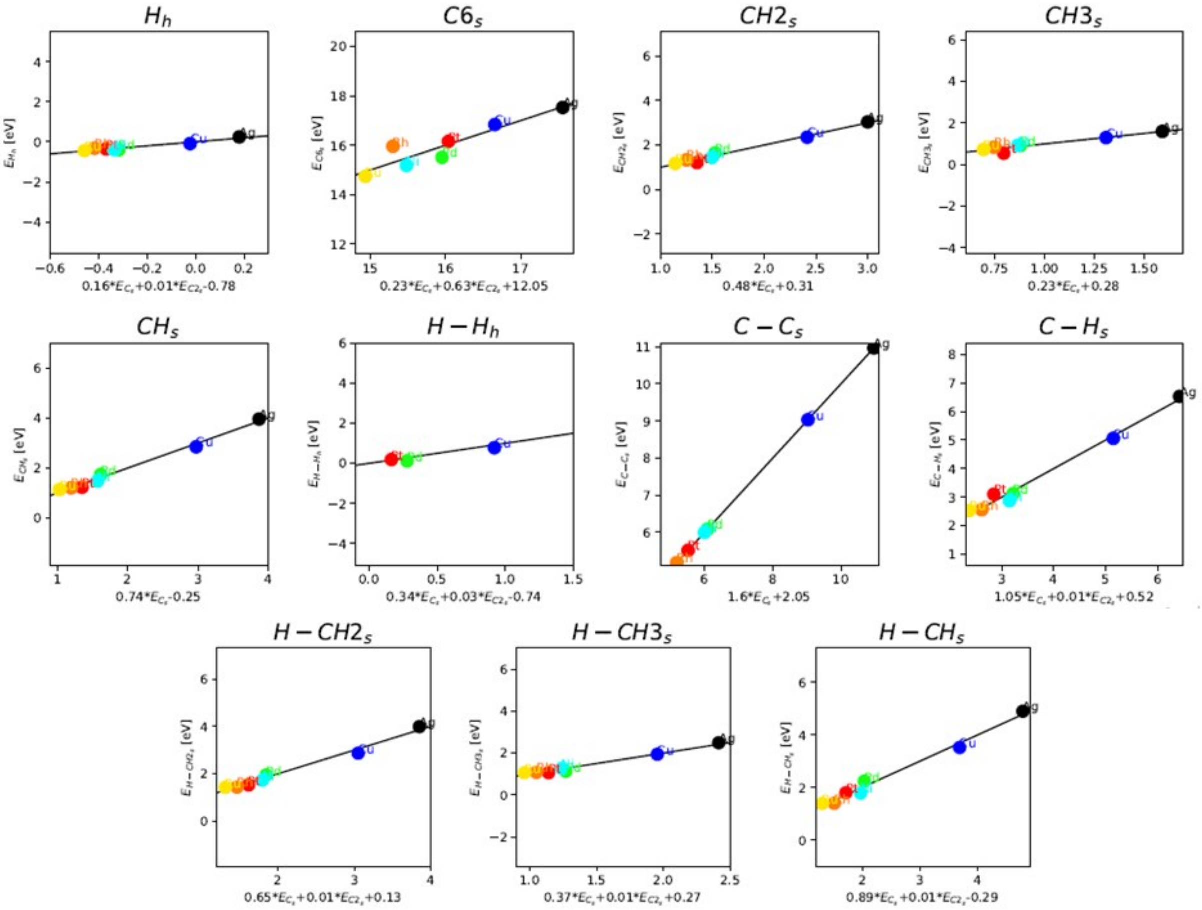

**Fig. S9.** Adsorption energy and Transition state energy scaling with the descriptors. Color code: Ag (black), Cu (blue), Pd (Green), Pt (Red), Rh (Orange), Ni (sky-blue), Ru (Yellow).

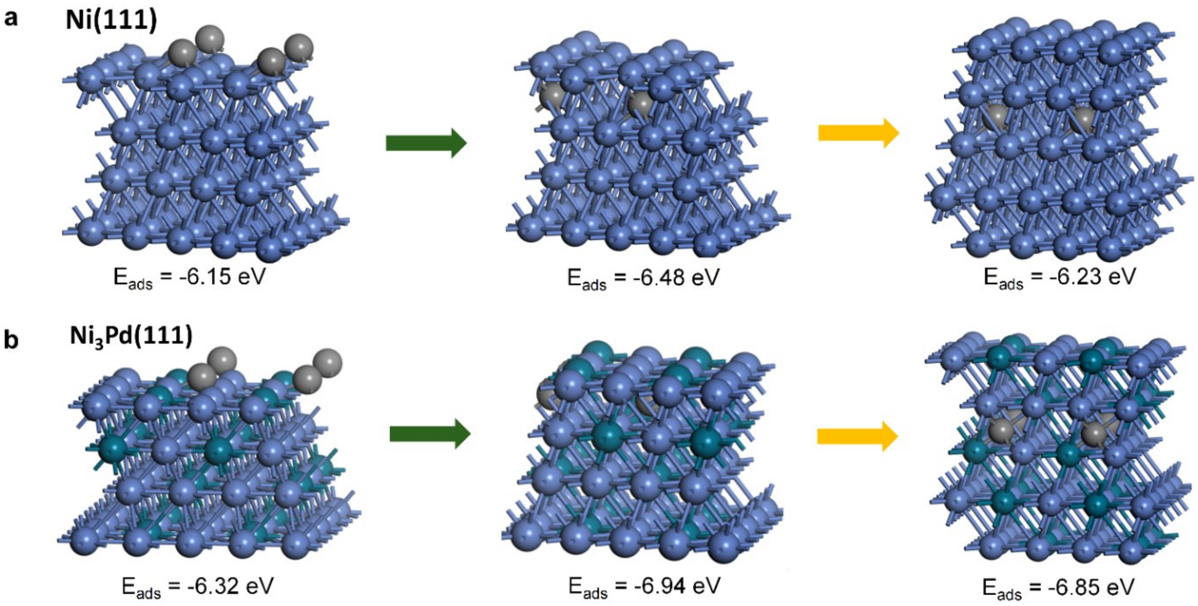

**Fig. S10.** Diffusion of surface carbon atom to the first and second sublayer of **a)** Ni(111) and **b)** $Ni_3Pd(111)$ surfaces.

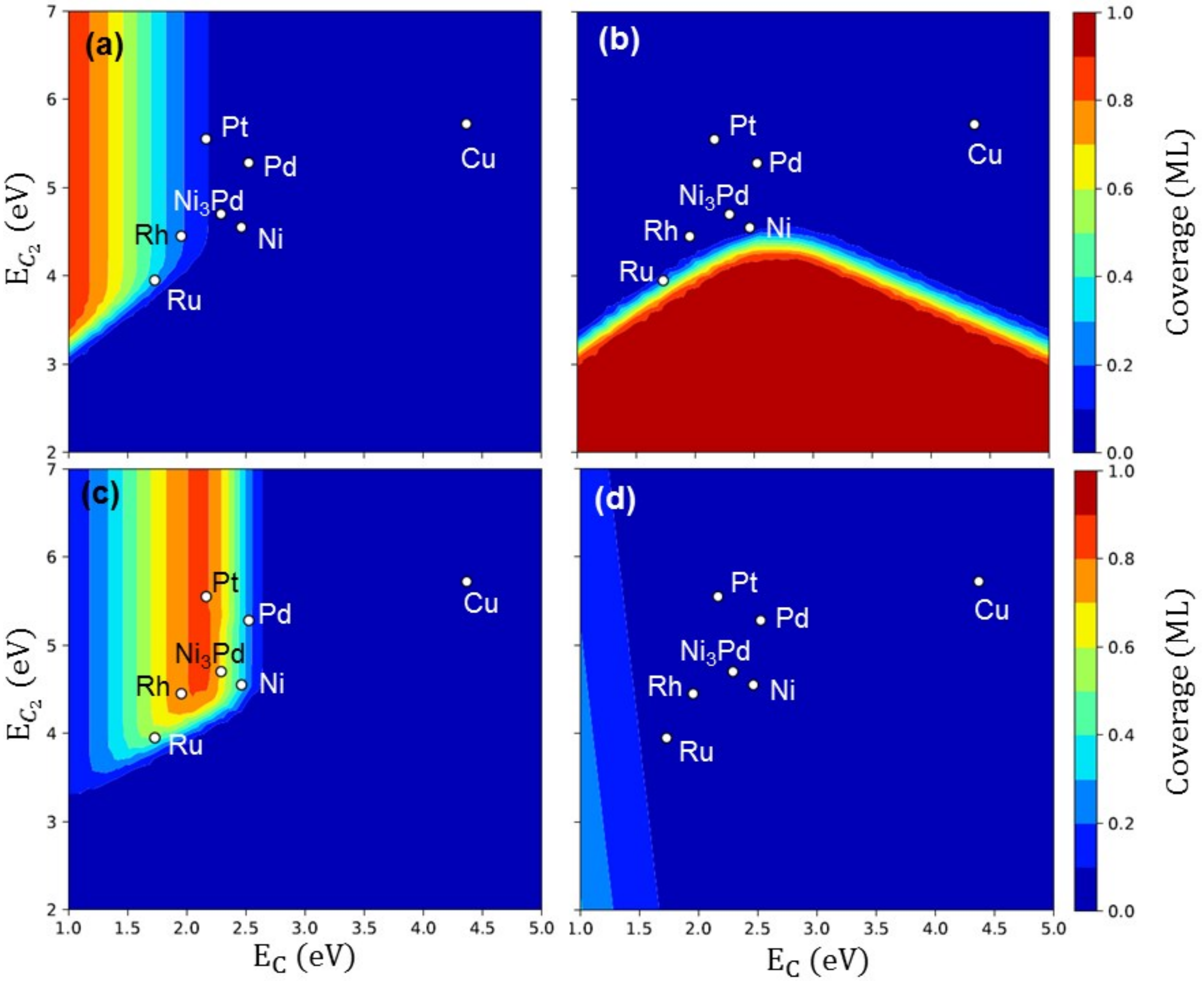

**Fig. S11.** Coverages **a)** C, **b)** $C_2$, **c)** CH and **d)** H over the transition metal (111) surfaces plotted against the C and $C_2$ binding energy. Reaction conditions: Temperature at 600 °C, Pressure = 1 bar $CH_4$, 0.01% conversion.

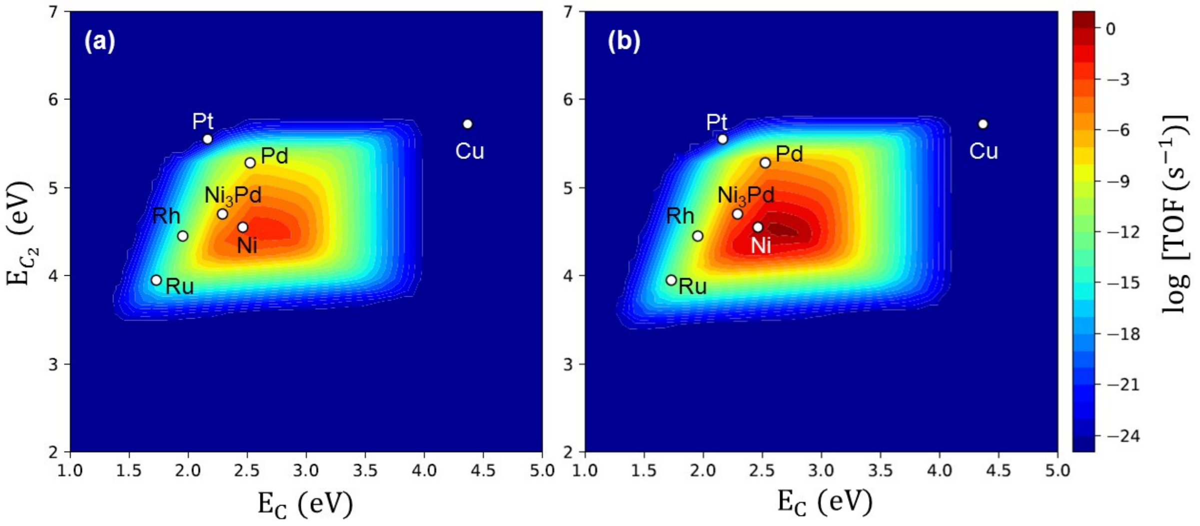

**Fig. S12.** Rate volcano plot for **a)** Coke and **b)** $H_2$ production over transition metal surfaces plotted against the C and $C_2$ binding energy. Reaction conditions: Temperature at 600 °C, Pressure = 1 bar $CH_4$, 0.01% conversion. The rates for $H_2$ and $C_6$ formation are 2 and 1/6 times of $CH_4$ dissociation rates.

## S3. Preliminary Technoeconomic Analysis

To assess commercial viability, we developed a process model using Aspen Plus V10 and conducted the preliminary techno-economic analysis. Figs. S13 depict the block flow diagram. Natural gas (NG) is converted into hydrogen and solid carbon nanomaterials via TCD reaction using a supported 10wt% Ni- 1wt% Pd catalyst at 600°C and 2.5 bar. Gas-phase product is compressed and sent to pressure swing adsorption (PSA) for $H_2$ separation. A portion of the unconverted NG is used to supply heat for the endothermic TCD reaction, and the rest is recycled back to the TCD reaction. Solid-phase product is sent to acid wash and carbon recovery. Leached Ni and Pd metals are recycled to generate fresh catalyst by impregnation, calcination, and reduction. For comparison purpose, process models for conventional steam reforming (SR) processes with and without carbon capture and storage (SR+CCS) are also evaluated.

Techno-economic analysis was then conducted for a scale of 100,000 $kg_{H_2}$/day for centralized $H_2$ generation. Key performance and economic metrics are presented in Table S2. The economic analysis was conducted in 2014 pricing basis with a natural gas price of \$0.25/kg (\$5.2/MMBtu). As shown in Table S2, the NG consumption and thermal efficiency of the TCD process is lower than that for both the SR and SR+CCS processes because of the production of by-product carbon. If the heating value of carbon by-product is included in the analysis, the efficiency of the TCD process will be higher than that of SR. The $CO_2$ emissions in TCD are 85% lower than that of conventional SR (1.67 and 9.6-11.5 $kg_{CO_2}/kg_{H_2}$), and 45% lower than that of SR+CCS (2.98 $kg_{CO_2}/kg_{H_2}$). The $CO_2$ emission is non-zero because part of the NG is used to supply the heat required by the endothermic TCD reaction; however, it could be further reduced by using $H_2$ as the heat source. Electricity consumption for TCD is higher than for SR even with on-site electricity generation from waste heat. This is primarily due to the large pressure difference required in the $H_2$ purification unit. A relatively large compressor is needed between the reactor and PSA unit since the reactor must be operated at relatively low pressure due to the equilibrium constraints. But this can be improved when operated at relatively higher temperature for higher conversion. It is noted that the validity of CCS is still controversial, as a result SR + CCS could be very high depending on geographical locations.

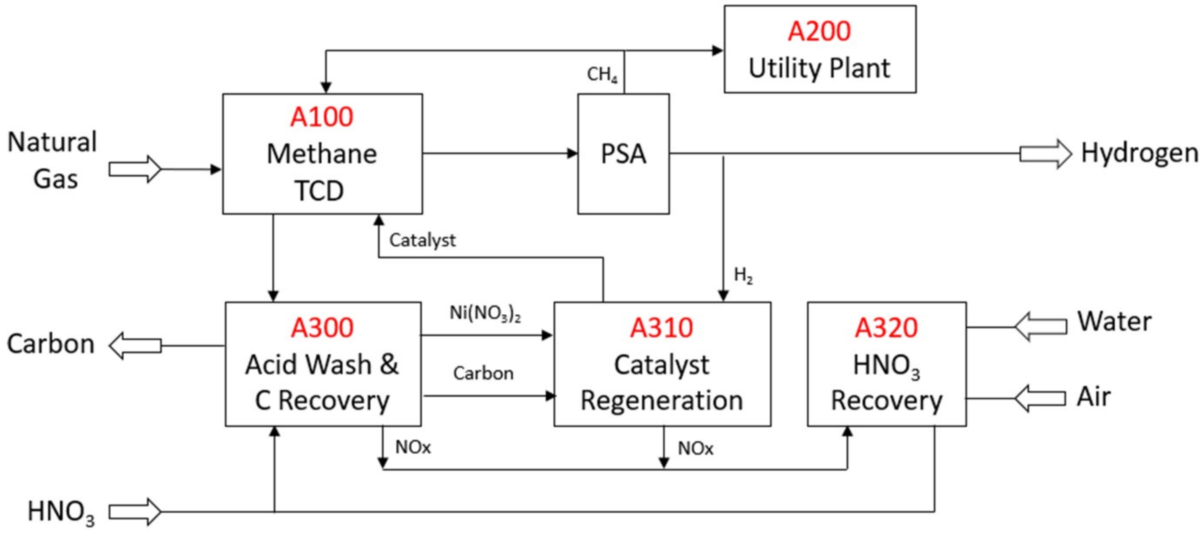

**Fig. S13.** Block flow diagram of the methane TCD process for CNT and $H_2$ production.

**Table S2** | Key performance for the methane TCD and SR processes

| | Raw Material | | Utility | Byproduct | Performance |
|---|---|---|---|---|---|
| | Natural gas (kg/kg$H_2$) | $HNO_3$ (kg/kg $H_2$) | Electricity (kWh/kg $H_2$) | Carbon (kg/kg $H_2$) | $CO_2$ Emission (kg/kg $H_2$) |
| SR (a, b) | 3.42 | | 0.28-2.10 | | 9.6-11.5 |
| SR+CCS (c) | 3.68 | | 0.60 | | 2.98 |
| TCD | 4.65 | 0.18 | 3.13 | 3.05 | 1.67 |

(a) PEP Yearbook, Hydrogen production by steam reforming of natural gas, 1E-586, 2014.

(b) PEP Yearbook, Hydrogen small scale by steam reforming, 1E-573, 2014.

(c) NREL, case study: central natural gas, future central hydrogen production from natural gas with $CO_2$ sequestration version 3, 2018.

Table S3 indicates that the proposed technology has the potential to produce $H_2$ economically if sufficient value can be obtained from the carbon byproduct (i.e., CNT or CNF). Preliminary results in Figure 2 shows that when setting $H_2$ price at \$2/kg $H_2$ for all three processes, selling carbon byproduct at \$1.37 /kg will make TCD comparable with SR and SR + CCS. A report highlighted the market size and the value of different type of carbons especially the carbon nanomaterials produced from the TCD[19]. According to this report, CNTand CNF or crystalline carbon can be sold at higher price. It is worth noting that, in Table 3, the capital cost for TCD is conservative, not optimized. Finally, government incentives in the form of carbon ($CO_2$) taxes would also assist in its economic competitiveness. Recent decarbonization initiative from U.S. has caused the demand on the low carbon fuel[20]. If the initiative becomes policy, SR process has to be connected to CCS which is very difficult to proactice. As a result, industry is looking for alternative hydrogen production approach without emitting $CO_2$. Methane pyrolysis is one of option.

**Table S3.** Key economic metrics for methane TCD and SR processes at different scales

| | TCD | SR | SR+CCS(3) |
|---|---|---|---|
| Scale (kg $H_2$/day) | 100,000 | 100,000 | 100,000 |

| | | | |
|---|---|---|---|
| Carbon production rate (kg/day) | 3,025,500 | N/A | N/A |
| Total ISBL capital cost (MM$) | 434.1(5) | 132.6 | 225.49 |
| Raw material cost ($/kg $H_2$) | 1.20 | 0.70 | 0.70 |
| Utility + O&M cost ($/kg $H_2$) | 0.76 | 0.21 | 0.35 (2) |
| Other cost (1) ($/kg $H_2$) | 2.25 | 0.80 | 0.80 |
| Minimum carbon selling price ($/kg @ $2.0/kg $H_2$ price) | 1.37(4) | | |

(1) Including plant overhear, taxed and insurance, depreciation, general and administrative, sales and research cost.

(2) The operating and capital costs of the CCS section was reported by NREL, case study: central natural gas, future central hydrogen production from natural gas with $CO_2$ sequestration version 3, 2018.

(3) It is noted that the validity of CCS is still controversial. Capital and operating cost may be much higher than cited by this study

(4) CNT/CNF are crystalline carbons which can be converted into carbon composite, polymer additives, electrode and sold at much higher than minimum selling price[19].

(5) This is not optimized still need improvement

## S4. References

[1] A.J. Medford, C. Shi, M.J. Hoffmann, A.C. Lausche, S.R. Fitzgibbon, T. Bligaard, J.K. Nørskov, Catal. Letters. 145 (2015) 794–807. https://doi.org/10.1007/s10562-015-1495-6.

[2] A.J. Medford, A.C. Lausche, F. Abild-Pedersen, B. Temel, N.C. Schjødt, J.K. Nørskov, F. Studt, Top. Catal. 57 (2014) 135–142. https://doi.org/10.1007/s11244-013-0169-0.

[3] https://github.com/SUNCAT-Center/catmap, (n.d.).

[4] L.C. Grabow, Computational Catalyst Screening, 1st ed., The Royal Society of Chemistry, 2014.

[5] F. Jalid, T.S. Khan, F.Q. Mir, M.A. Haider, J. Catal. 353 (2017) 265–273. https://doi.org/10.1016/j.jcat.2017.07.018.

[6] T.S. Khan, S. Hussain, U. Anjum, M. Ali Haider, Electrochim. Acta. 281 (2018) 654–664. https://doi.org/10.1016/j.electacta.2018.05.205.

[7] T.S. Khan, F. Jalid, M.A. Haider, Top. Catal. 61 (2018) 1820–1831. https://doi.org/10.1007/s11244-018-1028-9.

[8] J.S. Hummelshøj, F. Abild-Pedersen, F. Studt, T. Bligaard, J.K. Nørskov, Angew. Chemie - Int. Ed. 51 (2012) 272–274. https://doi.org/10.1002/anie.201107947.

[9] H. Falsig, J. Shen, T.S. Khan, W. Guo, G. Jones, S. Dahl, T. Bligaard, Top. Catal. 57 (2014) 80–88. https://doi.org/10.1007/s11244-013-0164-5.

[10] E. Nikolla, A. Holewinski, J. Schwank, S. Linic, J. Am. Chem. Soc. 128 (2006) 11354–11355. https://doi.org/10.1021/ja0638298.

[11] M. Argyle, C. Bartholomew, Catalysts. 5 (2015) 145–269. https://doi.org/10.3390/catal5010145.

[12] V. Jourdain, C. Bichara, Carbon N. Y. 58 (2013) 2–39. https://doi.org/10.1016/j.carbon.2013.02.046.

[13] L.C. Grabow, F. Studt, F. Abild-Pedersen, V. Petzold, J. Kleis, T. Bligaard, J.K. Nørskov, Angew. Chemie - Int. Ed. 50 (2011) 4601–4605. https://doi.org/10.1002/anie.201100353.

[14] A.C. Lausche, A.J. Medford, T.S. Khan, Y. Xu, T. Bligaard, F. Abild-Pedersen, J.K. Nørskov, F. Studt, J. Catal. 307 (2013) 275–282. https://doi.org/10.1016/j.jcat.2013.08.002.

[15] J.K. Nørskov, F. Studt, F. Abild-Pedersen, T. Bligaard, John Wiley & Sons, Inc., Hoboken, New Jersey, 2014.

[16] J.K. Nørskov, F. Abild-Pedersen, F. Studt, T. Bligaard, Proc. Natl. Acad. Sci. U. S. A. 108 (2011) 937–43. https://doi.org/10.1073/pnas.1006652108.

[17] T. Geißler, A. Abánades, A. Heinzel, K. Mehravaran, G. Müller, R.K. Rathnam, C. Rubbia, D. Salmieri, L. Stoppel, S. Stückrad, A. Weisenburger, H. Wenninger, T. Wetzel, Chem. Eng. J. 299 (2016) 192–200. https://doi.org/10.1016/j.cej.2016.04.066.

[18] M.W. Chase, NIST-JANAF Thermochemical Tables, 4th Edition, J. Phys. Chem. Ref. Data, Monogr. 9 (1998) 1–1951.

[19] R.A. Dagle, V. Dagle, M.D. Bearden, J.D. Holladay, T.R. Krause, S. Ahmed, (2017). An Overview of Natural Gas Conversion Technologies for Co-Production of Hydrogen and Value-Added Solid Carbon Products. ANL-17/11 | PNNL-26726

[20] https://www.usatoday.com/story/news/politics/2021/04/22/president-biden-pledge-reduction-us-greenhouse-gas-emissions/7307038002/